

Research Article

Control Strategy and Experiments for Robot Assisted Craniomaxillofacial Surgery System

Tengfei Cui,¹ Yonggui Wang ,¹ Xingguang Duan,¹ and Xiaodong Ma²

¹Beijing Advanced Innovation Center for Intelligent Robots and Systems, School of Mechatronic Engineering, Beijing Institute of Technology 5 Nandajie, Zhongguancun, Haidian, Beijing 100081, China

²The General Hospital of the People's Liberation Army, China

Correspondence should be addressed to Yonggui Wang; wangyg1025@163.com

Received 10 December 2018; Revised 10 February 2019; Accepted 7 March 2019; Published 27 March 2019

Guest Editor: Marie Muller

Copyright © 2019 Tengfei Cui et al. This is an open access article distributed under the Creative Commons Attribution License, which permits unrestricted use, distribution, and reproduction in any medium, provided the original work is properly cited.

Since the intricate anatomical structure of the craniomaxillofacial region and the limitation of surgical field and instrument, the current surgery is extremely of high risk and difficult to implement. The puncturing operations for biopsy, ablation, and brachytherapy have become vital method for disease diagnosis and treatment. Therefore, a craniomaxillofacial surgery robot system was developed to achieve accurate positioning of the puncture needle and automatic surgical operation. Master-slave control and “kinematic + optics” hybrid automatic motion control based on navigation system, which is proposed in order to improve the needle positioning accuracy, were implemented for different processes of the operation. In addition, the kinematic simulation, kinematic parameters identification, positioning accuracy experiment (0.56 ± 0.21 mm), and phantom experiments (1.42 ± 0.33 mm, 1.62 ± 0.26 mm, and 1.41 ± 0.30 mm for biopsy, radiofrequency, and brachytherapy of phantom experiments) were conducted to verify the feasibility of the hybrid automatic control method and evaluate the function of the surgical robot system.

1. Introduction

With the development of modern medical technology and the application of new technology in clinical practice, robot-assisted surgery is widely used as supportive tool for diagnosis, operation planning, and treatment in surgical intervention. Robot assisted puncture surgery is being increasingly accepted as an alternative treatment for cancer patients for surgery, especially in biopsy, thermal coagulation, and brachytherapy [1–3]. This way benefits patients with advantages of functional saving, symptomatic palliation, and local disease control. The puncture surgeries for craniomaxillofacial region usually are performed by doctors, relying on plentiful clinical experience or various image navigation devices. The intricacy anatomic structure, the extremely irregular shape, and evident personalized feature in maxillofacial surgery bring great challenge to surgical operation [4]. In craniomaxillofacial lesions, especially recurrent maxillofacial cancer, although some experienced surgeon performing the procedure could reduce the potential risks and have some functional results by using commercialized surgery

navigation system [5], such as BrainLab, intraoperative accurate puncture is still difficult for many doctors because of the complex tissue structure and requirements of high accuracy puncture.

Minimally invasive surgical procedures in craniomaxillofacial regions involve tumor biopsy, radioactive seeds brachytherapy, and radiofrequency thermal coagulation. Maxillofacial tumor, especially in skull base region, is one of the most common diseases and early diagnosis is important for treatment. With advance of minimally invasive surgery, needle biopsy has become a widely used method for early diagnosis. Radioactive seeds brachytherapy is well suited for skull base tumor because, unlike traditional radiotherapy, it does not use very high dose rates and is less likely to harm critical organs. At present the procedures of brachytherapy are associated with exposure to radiation. Radiofrequency thermal coagulation faces many challenges including deep oval foramen, long puncture path, complex anatomy, and high precision requirements. Surgeon manually locates the skin entry site of needle, adjusts the angulation of the needle, and negotiates the obstruction during the puncture. These

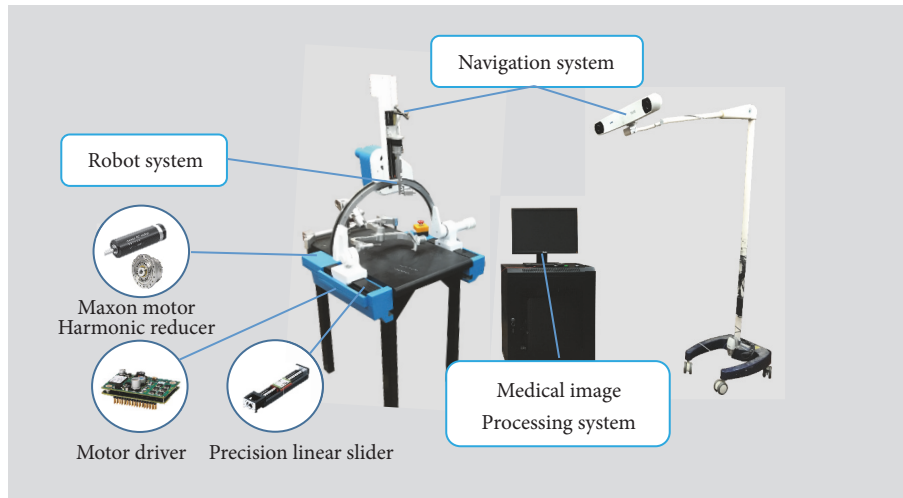


FIGURE 1: The presentation of robot assisted craniomaxillofacial surgery system.

can be great technical challenges for doctors. Needle puncture accuracy affects surgical treatment effect and may cause harm to the patient. Although technical assistance methods have been provided for needle puncture surgery, including conventional CT guide [6], individual template assistance, and image navigation [7], accurate needle placement still depends largely to a great extent on the surgeon's experience and hand-eye-mind coordination.

Surgical robots assisted craniomaxillofacial surgeries have developed rapidly nowadays, and advanced control technology and computer advantages greatly improve the maxillofacial surgery, especially the complex anatomical structure. The integration of imaging and robotic technology as "the third hand and eye" of the surgeon can be greatly taken advantage of robotic operation, improve needle displacement accuracy, and automatically perform the needle operation. The robot technology is widely known as an important instrument in the maxillofacial surgery because of its increasing advantages, such as high accuracy, stability, and flexibility of control. In 1994 Kavanagh [8] used the image-guided Robodoc robotic system for the first time in preclinical trials in the field of oral and maxillofacial surgery on the sacrum. In 1998 an interactive surgical robot system OTTO for craniomaxillofacial, which was installed on a surgical ceiling, was introduced by Lueth and Hein for drilling or cutting [9]. Genden et al. used Da Vinci robot to complete 9 cases of postoperative repair and reconstruction of tumors [10]. In 2010 Selber conducted a series of studies on the reconstruction of oropharyngeal defect by using Da Vinci surgical robot, including 1 case of free forearm flap, 2 cases of free anterolateral thigh flap, and 1 case of facial artery myomucosal flaps [11]. Theodossy et al. [12] and Omar et al. [13] used robotic arms (FARO arms) to simulate orthognathic surgery in model surgery. Chen Liming et al. [14] combined the Yaskawa MOTOMAN SV3X robot with optical navigation in Japan to simulate the craniofacial deformity on the human skull. Boesecke et al. [15] simulated 48 robotic-assisted implant placements that can accurately locate the

position, direction, and depth of preoperatively designed implants and assist doctors in the preparation of implant nests. Sun et al. [16] used a 6-degree-of-freedom Mitsubishi robot to perform automated dental implantation. The results showed that the registration accuracy was (1.42 ± 0.7) mm, indicating the feasibility of robot-assisted implant surgery. The RobaCKa robot system was developed by University of Karlsruhe (TH) and University of Heidelberg for craniofacial surgical osteotomy [17]. Kawana et al. [18] developed a remote controlled haptic drilling robot for oral and maxillofacial system. In addition, craniomaxillofacial surgery assisted robots have conducted extensive research in tumor treatment and other surgeries [19–22].

In radioactive tumor brachytherapy surgery, radioactive seeds implantation can adversely affect the operator's health and the potential ill effects of radiation cannot be ignored [23–28]. The robot assisted puncture system could provide great convenience for doctor once it can automatically perform needle puncture, radioactive seeds delivery and keep the doctor at a safe distance from the radioactive seeds. At the same time, the doctor can visualize the procedure of needle puncture in real time and display it in the medical image system [29]. By comparing preoperative planning and postoperative images, the robot assisted surgery system could verify the operation effectiveness. So we have developed a robot assisted craniomaxillofacial surgery system and evaluated the feasibility and reliability of this robot system in phantom experiments.

2. System Overview

According to the function of the surgical robot system, the robot assisted craniomaxillofacial surgery system as shown in Figure 1 could be divided into three subsystems, including robot subsystem, navigation subsystem, and medical image processing subsystem.

Robot subsystem comprises a positioning mechanism for needle displacement and three end effectors for tumor

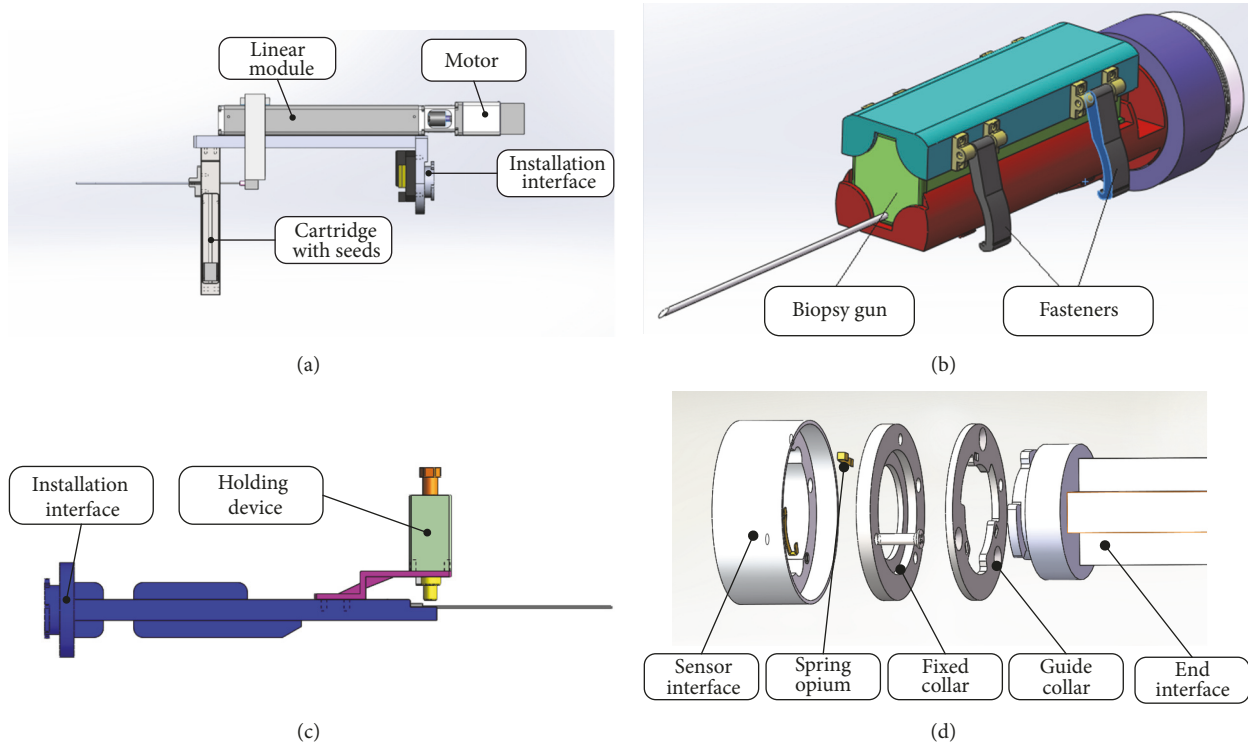


FIGURE 2: (a) Robot end effector for brachytherapy surgery; (b) end effector for biopsy surgery with clinical biopsy gun; (c) end effector for radiofrequency surgery with fast locking mechanism; (d) general interface explosion diagram.

biopsy, radioactive tumor brachytherapy, and radiofrequency thermal coagulation (Figure 1). In brief, the technical specifications of the robot system are as follows: (1) this weight is 15 kg, portable and remotely controlled, easy to be fixed to the operating table; (2) 5 degrees of freedom (DOFs) robot is used, with 3 DOFs for rotational motion, 1DOF for translational motion, and 1 DOF for surgical end effector operation. Rotating joint DOF consists of maxon motor and harmonic reducer; prismatic joint includes motor and precision linear slider. (3) Three operations correspond to three different surgical end effectors, and the universal interface at the robot fifth joint mounts quickly the end effectors to the robot with high accuracy. (4) Bus control system based on CANopen protocol completes robot joint control. (5) A 6-dimension force sensor (3813A SRI, Sunrise Instruments, Nanning, China) is fixed between the fifth joint and the end effector.

According to operation requirements, three end effectors (Figure 2) are designed, quickly installed, and disassembled to the robot end joint through the universal interface. In addition, the end effector for brachytherapy containing a cartridge with radioactive seeds was connected by a clamping slot connection, which facilitated easy removal and sterilization.

Navigation subsystem (Figure 3) realizes the registrations of various workspaces, obtained the transformational relationships between any robot workspaces, and provides real-time intraoperative navigation for surgery. An optical tracking system (Polaris, Northern Digital Inc., Waterloo, Canada) with 0.35 mm positioning accuracy and 20 Hz update rate

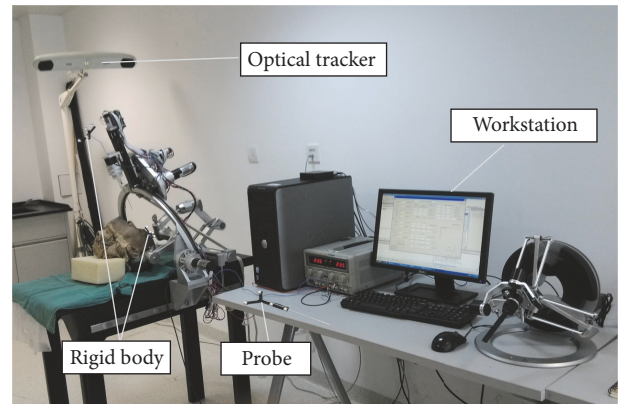


FIGURE 3: The presentation of navigation subsystem.

is focused that consisted of an optical tracker, one passive four-marker probe, and two passive four-marker rigid bodies. Two passive rigid bodies are fixed on the robot end effector and patient's head. In the surgical robot space navigation and positioning system, two import functions are surgical registration and intraoperative real-time tracking navigation. The optical tracker as measurement tool tracks the positions and orientations of probes and rigid bodies in real time.

Medical image processing subsystem includes the following features: 3D volume rendering of medical images, surgical scene control, 2D and 3D image segmentation, puncture

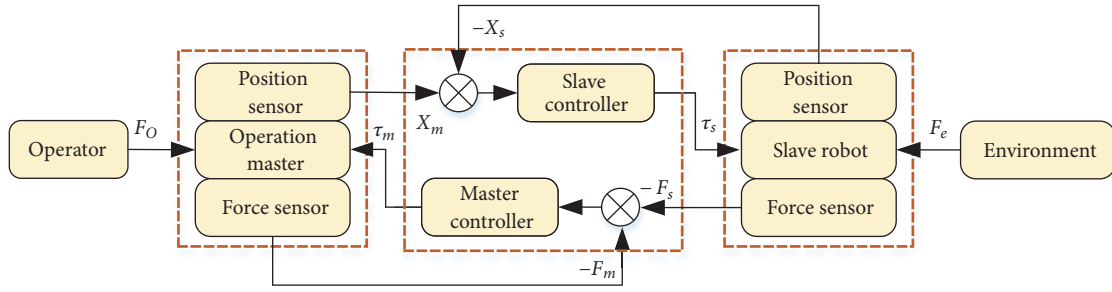


FIGURE 4: The control strategy of double-end force/position feedback.

path information processing, puncture path recommendation, postoperative verification, and evaluation. In addition, combining optical navigation system, real-time display of puncture needles in the image processing subsystem is displayed.

3. Control Strategy

In order to be convenient to the doctor's operation and reduce the learning time in which doctors operate surgical robot, the control system of surgical robot is designed from the perspective of human-computer interaction and operation procedure and is divided into two parts, automatic control for fine adjustment and master-slave control for passive positioning. Master-slave control mainly moves puncture needle from the starting point to the vicinity of entry point and remotely implants radioactive seeds. In master-slave mode, the robot's movement follows the doctor's hand, avoids collision with the patient's body, and positions the operation needle in the vicinity of the entry point [30, 31]. In automatic control mode, the robot achieves the precise positioning of the target point and completes the puncture process. The robot control hardware design mainly includes drive module (maxon motor and ACK-055-06 control driver of Copley, USA), CAN communication card (CAN-PCI-02 Copley), six-dimensional force sensor (3813A SRI, Sunrise Instruments, Nanning, China), and hardware circuit modules.

3.1. Master-Slave Control. The goal of the master-slave control is to obtain high transparency and provide good maneuverability. In the master-slave mode, the puncture needle could be controlled from current position to the vicinity of the entry point. The method is a more convenient operation, especially in the radioactive tumor brachytherapy surgery; this reduces the radiation received during the procedure. The doctor could complete radioactive tumor brachytherapy surgery by using remote operation. The master device (6 DOFs, omega.6 haptic device, Force Dimension, Switzerland) provides decoupling of translational and rotational motions, enabling gravity compensation, etc., and the slave device is the surgical robot. The doctor views the target and current pose of the puncture needle in real time, observes the movement of the robot, and prevents the puncture needle from interfering with the obstacle such as skull, fixed bracket,

or surgical instruments in the surrounding environment. The control strategy of double-end force/position feedback is used and has a good dynamic response, as shown in Figure 4.

The dynamic equation of the master could be expressed as follows:

$$\begin{aligned} F_o - \tau_m &= M_m s^2 X_m + B_m s X_m + K_m X_m \\ \tau_m &= K_f (F_m - F_s) \end{aligned} \quad (1)$$

where M_m , B_m , and K_m are the inertia, damping coefficient, and stiffness matrix of master device. F_m and F_s are the force values monitored from the master and slave force sensor. τ_m is the driving force of the master device. F_o is the force applied by the operator to the master device. X_m is the displacement vector. K_f is the force gain matrix. The dynamic equation of the slave could be displayed.

$$\begin{aligned} \tau_s - F_e &= M_s s^2 X_s + B_s s X_s + K_s X_s \\ \tau_s &= K_a (X_m - X_s) + K_v (X_m - X_s) \\ &\quad + K_p (X_m - X_s) \end{aligned} \quad (2)$$

where K_a , K_v , and K_p are the acceleration, speed, and position gain matrix of the slave. The dynamic equation and control strategy of the environmental could be expressed.

$$\begin{aligned} F_e &= - (M_e s^2 X_e + B_e s X_e + K_e X_e) \\ X_e &= -X_s \end{aligned} \quad (3)$$

M_e , B_e , and K_e , respectively, represent the inertia, damping coefficient, and stiffness matrix of the tissue environment. X_e is the position vector of the contact tissue environment. A constant transmission delay in the communication channel is considered. In the master-slave control strategy, the integral separation PID control algorithm is adapted and improves the speed response in stages. The method is that when the deviation is more than a given deviation, PID control is used to avoid overshooting and ensure the system's response speed. When the deviation is less than a given threshold, PID control is used to ensure the control accuracy. The method is to

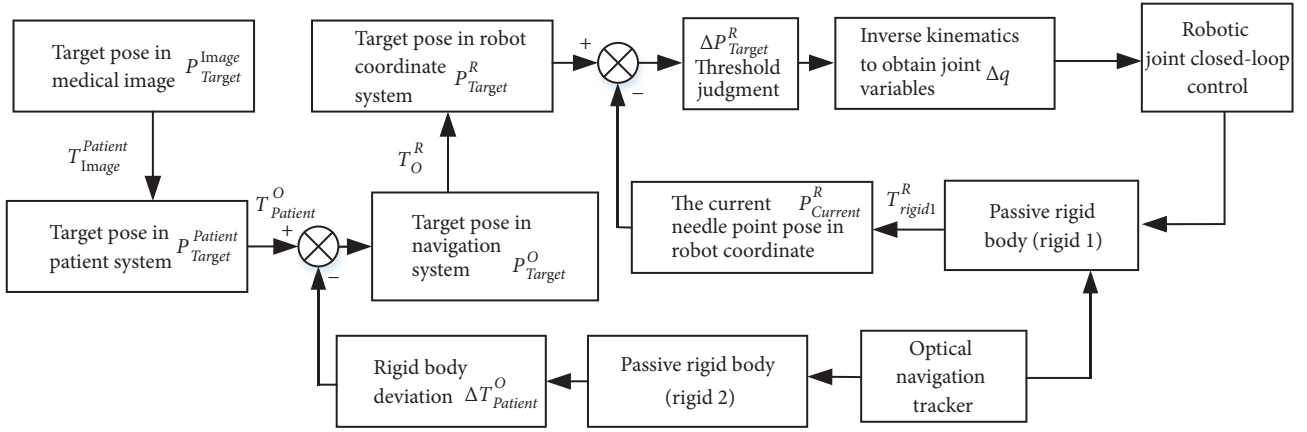


FIGURE 5: Robot navigation control system block diagram based on optical navigation.

multiply the integral term by a coefficient, and the value of the coefficient is 0 or 1 depending on the deviation.

$$u(k) = K_p e(k) + \beta \frac{T}{T_I} \sum_{j=0}^k e(j) + \frac{T_D}{T} [e(k) - e(k-1)] \quad (4)$$

$$\beta = \begin{cases} 1 & |e(k)| \leq \varepsilon \\ 0 & |e(k)| > \varepsilon \end{cases} \quad (5)$$

Through analyzing the control method of the PID method and combining the master-slave control algorithm, accurate and rapid control of the master-slave operation could be realized.

3.2. "Kinematics + Optics" Hybrid Automatic Motion Control.

Once the robot needle reaches the vicinity of the entry point during the execution of the surgery, the automatic motion control is chosen by doctor from the master-slave control. By the surgical planning software, the target pose of the puncture entry point is transmitted to the robot system and navigation system. The positioning accuracy of robot could be affected by the kinematics calculation, mechanical transmission, servo control, etc. In order to improve the positioning accuracy of the robot, the "kinematics + optics" hybrid motion control method is proposed. The robot inversely solves each joint movement angle through the inverse kinematic, and the target pose is converted into the navigation system through spatial registration relationships. The robot, which moves to the target point according to the operation plan, realizes accurate motion through the closed loop control of the joint encoder. Meanwhile, the pose quaternions from navigation system are used for pose correction. The pose needle and patient could be tracked and compensated in real time to ensure the accuracy of the puncture.

The robot automatic control system block diagram is shown in Figure 5. Firstly, the target point in the medical image system is converted into the real patient coordinate system. The navigation system is used to locate the position

of the patient in real time by the passive rigid body fixed to the patient, so as to compensate the deviation caused by the movement of patient. After the target pose is transmitted to surgical robot coordinate system, the robot moves to the target point by comparing with the real-time pose of the puncture needle tip as so to achieve accurate positioning of the target point.

The robot automatic control system includes two closed-loop controls; one is the servo control of the robot body system, that is single-joint servo control, and the other is global closed-loop control based on optical navigation. In robot automatic control, the global closed-loop control is achieved by real time acquisitions of optical navigation. P_{Target}^{Image} is the target pose in the medical image coordinate system. By the conversion relationship between the patient coordinate system and the image coordinate system, the target pose in the patient coordinate system can be obtained.

$$P_{Target}^{Patient} = T_{Image}^{Patient} P_{Target}^{Image} \quad (6)$$

The target point is converted from patient coordinate system to the optical navigation coordinate system, and the conversion relationship between the two coordinate systems has been determined in the spatial registration. Due to movements of the patient or optical navigation tracker during surgical operation, the transfer relationship is compensated through real-time navigation tracking. The target point in the navigation coordinate system P_{Target}^O is represented.

$$P_{Target}^O = (T_{Image}^O + \Delta T_{Image}^O) P_{Target}^{Image} \quad (7)$$

Before the robot moves to target point, the target position and orientation of robot will be transformed from navigation coordinate system to robot coordinate system. Also due to the movement of the robot or optical navigation the transfer relationship between them is compensated through real-time navigation tracking. Since the passive navigation rigid is installed at the end effector of the robot and the robot transfer relationship is based on the robot base coordinate system,

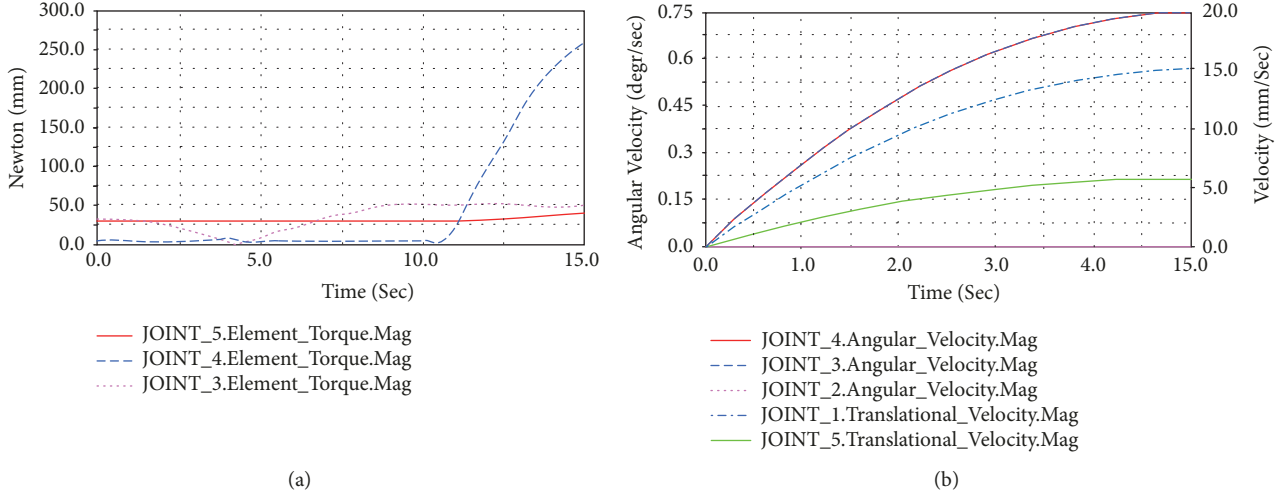


FIGURE 6: When the motion trajectory was given, the variation curve of force, velocity of the robotic joint could be obtained. The curves of three rotary joint driving forces (a) help to the drive unit selection; the variation curves of joint speed ensure the robotic flexible movement.

the robot joint angle values are determined by the inverse kinematics so that the deviation between the robot coordinate system and navigation coordinate system could be calculated. ΔT_O^R is the compensation parameter matrix, and the target point in robot base coordinate system could be listed.

$$P_{\text{Target}}^R = (T_O^R + \Delta T_O^R) P_{\text{Target}}^O \quad (8)$$

Through inverse kinematics calculation, the target point can be converted into the joint vectors of robot to control the robot motion. The position information of current puncture point in navigation coordinate system can be obtained by the real-time tracking of passive rigid body. The pose of current puncture point is converted to the robot coordinate system, and the closed-loop control can be achieved by comparing with the target pose in robot base coordinate system. $\Delta \bar{P}_{\text{Target}}^R$ is deviation between the current pose information of puncture point and the target pose in robot base coordinate system. The deviation can be adjusted by PID controller:

$$\begin{aligned} \Delta \bar{P}_{\text{Target}}^R &= K_p [\Delta P_{\text{Target}}^R(k) - \Delta P_{\text{Target}}^R(k-1)] \\ &+ K_I \Delta P_{\text{Target}}^R(k) + K_D [\Delta P_{\text{Target}}^R(k) \\ &- 2\Delta P_{\text{Target}}^R(k-1) + \Delta P_{\text{Target}}^R(k-2)] \end{aligned} \quad (9)$$

$$\bar{P}_{B\text{Target}(k)}^R = \bar{P}_{B\text{Target}(k-1)}^R + \Delta \bar{P}_{B\text{Target}(k)}^R \quad (10)$$

where K_p is the proportional gain, K_I is the integral gain, K_D is the derivative gain, k is the sampling sequence, and $k = 0, 1, 2, \dots, n$. $\Delta \bar{P}_{\text{Target}}^R$ is the increment of deviation at the k sampling time. $\bar{P}_{B\text{Target}(k)}^R$ is the output of the PID controller at the k sampling time. The optimal deviation is obtained by adjusting the gain parameters of PID controller. Thus, the joint angles can be calculated by inverse kinematics to control the robot to reach the target position.

4. Simulation and Experiments

4.1. Kinematic Simulation. The simulation aims to express the process of robot running and then ensures the velocity and acceleration of motion joints in the process of continuous motion. The method of simulation is analyzing mechanical property to single component with application of Newtonian mechanics, establishing the relationship of force and velocity under certain restraint condition. Once setting the robot and the motion trajectory, the postprocessor module of Adams could be used to analyze robot joint force and velocity as shown in Figure 6. It is significant to optimize the structure and hardware selection of robot.

4.2. D-H Parameter Identification. According to the correction of the D-H parameter model of the robot, there are certain errors in the parameters of the robot due to the factors such as processing, assembly, and environments. The geometric method and fitting method are adopted for the D-H parameter identification. The zero position of robot is determined by geometric method and the initial kinematics D-H parameter of the robot is given. Then, the D-H parameters are corrected by using the fitting method. The parameter identification for measuring tool uses FARO measuring arm (FARO Edge, FRAO Technology, Inc.).

The FRAO measuring arm is fixed near the surgical robot to ensure that the measuring points could cover the operating space of the surgical robot. The origin positions of each joint coordinate system of the robot kinematic model are obtained by fitting spatial point sets. The method is to control each joint of robot to move to different positions and to obtain the coordinates of the marker points on the end effector using the probe of the FARO measurement arm at each position. The corresponding joint axis directions are calculated by fitting these measurement points. Then the initial D-H parameters could be got by the corresponding joint coordinate origins positions.

TABLE 1: The D-H parameter identification results.

Joint	α_i (o)	d_i /(mm)	a_i /(mm)	θ_i (°)	Range
1	90.75	d_1	-0.08	0.052	-200~200 mm
2	0.02	0.04	0.13	θ_2	-80°~50°
3	-0.06	0.021	403.26	θ_3	-60°~60°
4	-89.53	-0.10	0.074	θ_4	-70°~70°
5	0.09	d_4	-0.06	0.04	0~200 mm

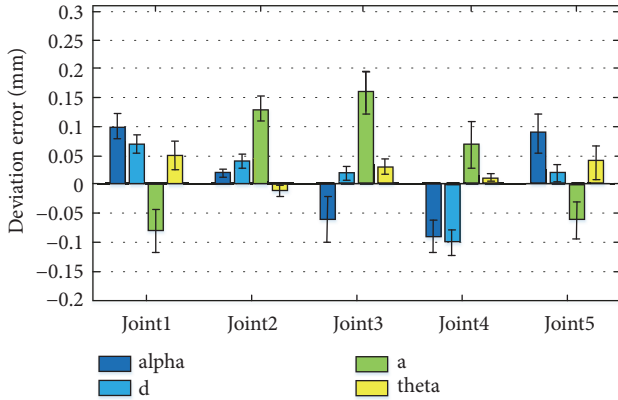


FIGURE 7: The identification errors of each joint's D-H parameters. 20 points were selected as a group to solve D-H identification parameters and 5 trials were performed to obtain the mean and standard deviation.

The deviation of the transformation matrix of the robot link is the difference between the actual transformation matrix ${}^jT_i^R$ and the nominal transformation matrix ${}^jT_i^N$.

$$\begin{aligned}
 d\left({}^jT_i^N\right) &= {}^jT_i^N - jT_i^R \\
 &= \frac{\partial {}^jT_i^N}{\partial \theta_i} \delta \theta_i + \frac{\partial {}^jT_i^N}{\partial d_i} \delta d_i + \frac{\partial {}^jT_i^N}{\partial a_i} \delta a_i \\
 &\quad + \frac{\partial {}^jT_i^N}{\partial \alpha_i} \delta \alpha_i
 \end{aligned} \quad (11)$$

A certain threshold of the deviation between the theoretical pose value and the actual pose value in the measurement coordinate system is set. Once the threshold satisfies the conditions, the parameter deviation vector could be obtained. 20 point coordinates in the measurement coordinate system and the corresponding joint angles are recorded. The iterative least squares method is used to obtain the deviation of the joint coordinate system parameters. 5 trials for each of 20 points were performed and averaged in Figure 7. The correction value of the D-H parameters is calculated in Table 1.

4.3. Positioning Accuracy Experiments. Robot positioning accuracy experiments are the verification of the controlled

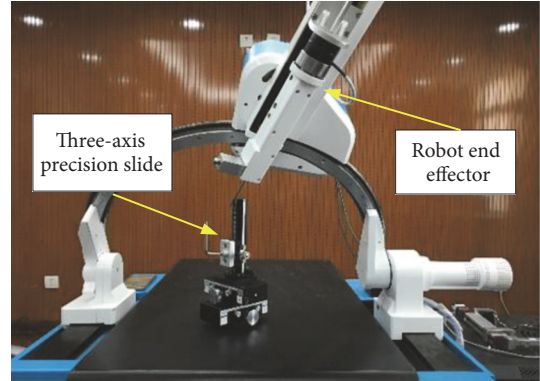


FIGURE 8: The positioning error experiments based on open-loop control and hybrid automatic control.

positioning of the surgical robot system. These have been implemented in open-loop robot control mode and “kinematics + optics” hybrid control mode based on navigation system. The feasibility of “kinematics + optics” hybrid automatic motion control could be verified. In order to calculate the influence of errors such as 3D medical image reconstruction and registration algorithm, the target point coordinates are obtained directly by using the passive probe of the optical navigation in the experiment. The three-axis precision slide (K301-30LMS-4 Suruga Seiki Co., Ltd., Accuracy 0.1mm) is used as the measurement tool as shown in Figure 8. The predetermined target positions coordinates are recorded by the optical measuring probe from the end point of the three-axis precision slide.

In the positioning accuracy experiment of open-loop robot control mode, the angle differences of each joint are calculated by analyzing the pose deviation between the target position and the current position. Then the robot reaches the target point through the motor servo control. The positioning error of open-loop control mode could be calculated by comparing Euclidean distance between the position of the needle tip and the target point.

In the positioning accuracy experiment of hybrid control mode, the passive rigid body is fixed at the end-effector of robot. The optical tracker is placed in a representative location to achieve the best positioning effect. The “kinematics + optics” hybrid motion control method is applied to the motion control of robot. The needle tip of robot is controlled to move to predetermined target positions, and

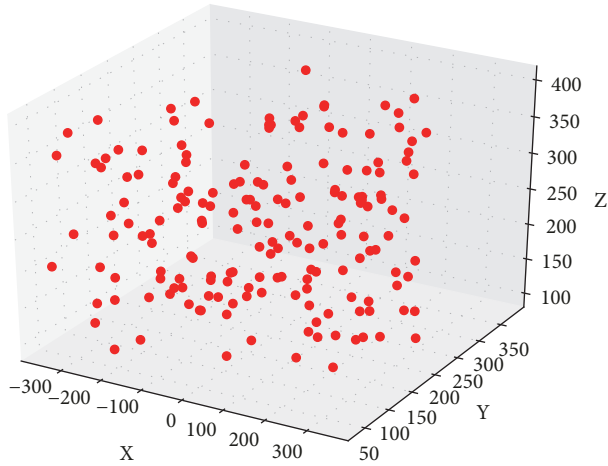


FIGURE 9: Test point distribution map in the workspace.

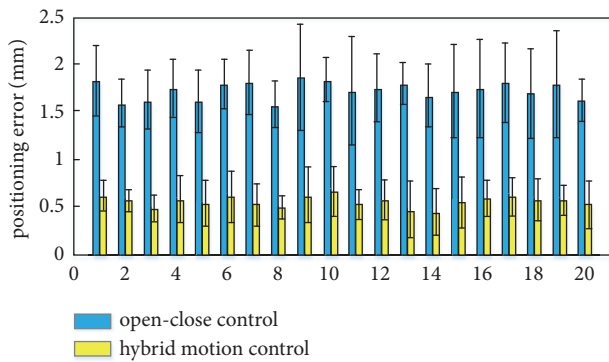


FIGURE 10: Comparing the positioning error between open-loop mode and hybrid motion control mode; each bar shows the mean and standard deviation of 10 trails for each of 20 preset location points.

its coordinates are recorded by the three-axis precision slide simultaneously. Then the positioning error of robot based on “kinematics + optics” hybrid motion control method can be obtained. In order to ensure the accuracy of the operation in actual operation, the maximum speed is operated at a distance of 3 cm from the target point. Within 3 cm from the target point, the needle point speed is controlled to be less than 0.02 m/s.

In order to ensure the effectiveness of the robot operation in the workspace, we randomly grabbed 200 points in the workspace in Figure 9 and divided them into 10 groups, 20 points in each group. Control the puncture needle from the same starting position to the target position in open-loop and “kinematic + optics” hybrid motion control mode in each group.

Figure 10 shows the positioning error for each of 20 preset points, when performing the experiments in open-loop control mode and hybrid motion control mode. The 10 trials were implemented to verify two control modes. The positioning error of open-close control mode is $1.73 \pm$



FIGURE 11: The setup of phantom experiments of biopsy, radiofrequency, and brachytherapy, including navigation system, control station, surgical robot, and phantom.

0.46 mm, while the hybrid mode control is 0.56 ± 0.21 mm. The reason is mainly the repetitive error of robot installation, robot D-H parameter error, registration error, etc. The hybrid motion control could reduce the impact of above error on the experimental results.

4.4. Phantom Experiments of Biopsy, Radiofrequency, and Brachytherapy. In order to verify the error of the robot-assisted puncture surgery system, the phantom experiments of biopsy, radiofrequency, and brachytherapy were conducted as shown in Figure 11. The skin was simulated by plasticine and the puncture target made with meat balls was buried inside the phantom. For different operations, the corresponding end effector was chosen. In the brachytherapy phantom experiment, the stainless steel wires of 1 mm diameter and 5 mm length were used instead of radioactive seeds to avoid radiation to the operators. All experiments were performed in the department of oral and maxillofacial surgery (Peking University School and Hospital of Stomatology). The study was approved by the local ethics committee.

The preoperative planning coordinates and postoperative seeds position were aligned by matrix transformation after image fusion, using the ICP algorithm. The total error was defined as the Euclidean distance calculated by the offsets of the coordinates. 30 trails of biopsy phantom experiments were performed and the mean placement error was 1.42 ± 0.33 mm. In the radiofrequency thermal coagulation phantom experiment, the mean placement error corresponding to 20 groups was 1.62 ± 0.26 mm. In the radioactive tumor brachytherapy phantom experiment, a total of 100 seeds were deposited by the robot system. The mean placement error was 1.41 ± 0.30 mm in phantom experiments ($p < 0.005$). The results of experiments were shown in Figure 12.

The cause of the errors includes the following: the layer spacing of the CT device, the 3D reconstruction image algorithm, the registration algorithm, robot control positioning error, and needle deformation. From the experiments data, the reason that the error of radiofrequency experiment is more than biopsy and brachytherapy is the longer puncture depths. The effect of brachytherapy experiment is analysis by the treatment planning system and shows that the radioactive dose map deviation is less than 1%, which is a reasonable seeds implantation as shown in Figure 13.

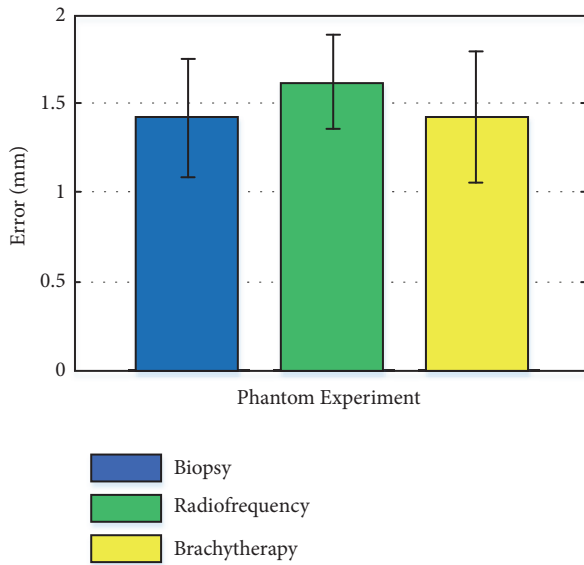


FIGURE 12: The accuracy of phantom experiments of biopsy, radiofrequency, and brachytherapy.

5. Conclusions and Discussion

This paper presents a robot assisted craniomaxillofacial surgery system through the analysis of surgical requirements. Motion performance analysis was conducted to validate the flexibility and feasibility of robot system. The hybrid automatic control for active fine adjustment and master-slave control for passive positioning were designed to build robot control system. In addition, the kinematic simulation and D-H parameter identification experiments were conducted to verify robotic precise manipulation. Positioning accuracy and phantom experiments of biopsy, radiofrequency, and brachytherapy demonstrate that the robot assisted surgery system could have accurate puncture effect.

From the perspective of human development and clinical application, laparoscopic robots, orthopedic robots, vascular interventional robots, and targeted puncturing robots are several important directions. The positioning of the puncture needle is achieved relying on the high precision and stability of the robot [32, 33]. Its application scope includes neurosurgery, craniomaxillofacial puncture, lung, liver, and other organs' percutaneous puncture. Robot-assisted puncture surgery systems are generally composed of surgical robots, medical image planning and processing, and surgical navigation systems, which are, respectively, "hand", "brain," and "eye" of the entire system. In order to provide doctors with a wider vision field and simplify surgical procedures, the surgical robots that are visualized, of lightweight, and easy to integrate with CT/MR devices have begun extensive research. Some puncture robot systems have been commercialized and completed a series of clinical operations in specific areas. At present, commercialized puncture robot systems such as the MAXIO robot system (Perfint Healthcare Pvt. Ltd) are placed near to the CT bed and are controlled to move to the target

point through the surgical planning. In addition, there are ROSA from Medtech in France [34], Renaissance from Mazor Robotics in the United States, Pathfinder from Pathfinder Technologies [35], NeuroMate robotics from Renishaw in UK [36], B-Rob from ISYS Medizintechnik GmbH [37], etc. These systems have already demonstrated certain clinical effects.

In our positioning accuracy experiments, the navigation probe was used to specify the target point. The robot positioning error is analyzed by comparing the specified target point and the actual position of the needle tip. The coordinates of the two measuring points must be in the same coordinate system. It is difficult to measure the coordinates of the puncture tip using an optical navigation probe. So the three-axis precision slide (K301-30LMS-4 Suruga Seiki Co., Ltd., Accuracy 0.1 mm) is chosen to measure coordinates. In order to facilitate the measurement of the coordinates of the needle tip of the puncture needle, a cylindrical rod with a cross section pit is connected to the end of the three-axis precision slide. 20 points, whose positions could be measured by precision slides, are selected for positioning accuracy experiments as much as possible into the robot's entire workspace. The 10 trials were implemented to verify two control modes. The positioning error of open-close control mode is 1.73 ± 0.46 mm, while the hybrid mode control is 0.56 ± 0.21 mm. The reason is that the repeated positioning errors in robotic installation beds are variable, and the registration error between robot and navigation system is also present. The "kinematic + optical" hybrid motion control method utilizes the characteristics of optical navigation real time closed-loop control and kinematics to achieve closed-loop robot control.

In phantom experiments, different materials have been used to simulate soft tissue, with most studies using gels and polyvinyl chloride, which cannot really simulate the complexity of the tissues of the maxillofacial region. During the surgical procedure, the surgical end effectors are replaced as required. If the universal interface generates increased error when replacing the surgical actuator, the surgical robot puncture needle needs to be recalibrated. Therefore, the error experiment about replacing the robot end effector was conducted. The average value of replacing error of the biopsy end effector is 0.307 mm, and the standard deviation is 0.157 mm. The radiofrequency end effector is 0.348 mm and the standard deviation is 0.238 mm. The brachytherapy is 0.164 mm and the standard deviation is 0.091 mm. The phantom experiment study had some drawbacks, as neither plasticine nor meat balls used as targets exhibit significant anisotropism or simulate the complex behavior of soft tissues. The skin was simulated by plasticine and the puncture target was made with meat balls. Compared with the puncture accuracy experiments, the puncture errors caused by the phantom experiments mainly include the following: the layer spacing of imaging equipment, the 3D reconstruction image algorithm, the registration algorithm, the robot control positioning error, and puncture needle deformation caused by plasticine [38]. In addition to the phantom experiment, we also carried out cadaveric experiment on this prototype. The surgical robot finished the needle placement and automatic

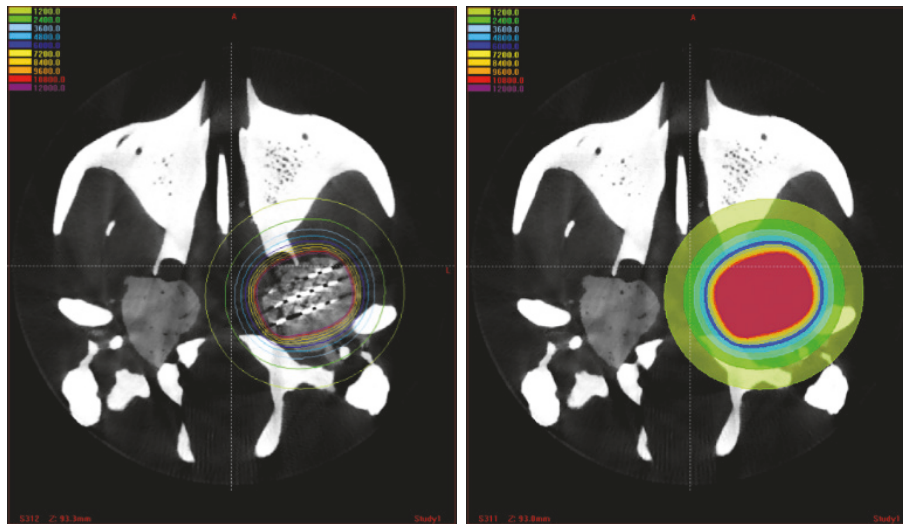


FIGURE 13: The analysis of the radioactive does map deviation.

puncture. In the cadaveric experiment, the average error of biopsy puncture is 2.58 mm, the standard deviation is 0.61 mm, and the tissue can be taken in the biopsy gun for each puncture. The average error of radiofrequency thermal coagulation surgery is 3.17 ± 0.94 mm; one of the 20 experiments failed to pass through the foramen ovale. The average error of the brachytherapy is 2.83 ± 0.50 mm; the TPS system analysis shows that the radioactive dose topographic map deviation was less than 5%.

The needle deformation is an important challenge for robot assisted puncture. The most commonly used oblique tip puncture needles in clinical practice are nickel-titanium alloy materials, which have high elasticity. In the process of soft tissue puncture, there is a needle deflection due to the asymmetry of the needle tip. A reasonable explanation is that needle deflection was primarily responsible for needle displacement with simulated tissue or real tissue, as has been reported in previous studies [39, 40]. Although the hybrid motion control guarantees robot motion accuracy to 0.8mm, the performance of needles, which are vulnerable to be bendable, can bring external errors. At present, the deformation of the puncture needle caused by the soft tissue and the physiological movement of the human body becomes a bottleneck for the robot to achieve high precision puncture positioning. As the puncture needle advances in soft tissue, it receives various resistances from the soft tissue. For oblique flexible needle, the relationship between puncture force and needle deformation is studied to obtain the interaction mechanism, which can make the puncture process accurate, controllable, and safe.

For the difficulty of needle deflection, we carried out the theory and experimental study of needle deflection based on force perception as shown in Figure 14. The 18G and 20G flexible oblique-tip needles were used to puncture the phantom at different speeds. The camera took the puncture process and the puncture depth was 120 mm to analyze the difficulty of needle deflection. The flexible oblique-tip needle

is used so that the needle deflection can be presented more easily. The soft tissue phantom should be able to simulate good viscoelastic soft tissue characteristics. The phantom used in this puncture experiment was prepared by mixing gelatin powder with water in a certain proportion and refrigerating in a refrigerator at 4°C for 12 hours. Since the gel is prone to water loss and hardening, the experiment must be completed within 1 hour after being taken out from refrigerator.

Analysis of experimental results shows that the finer the puncture needle is, the larger the needle deflection is. By recording the puncture force, the theoretical model is used to analyze the offset of the flexible oblique-tip needle. The offset of the needle in the acquired image is compared with the theoretical analysis; the measured error is less than 1 mm. This work is still under study; experiments on multilayer soft tissue phantoms are continuing to be performed.

Although many efforts have been made to model needle insertion forces, it has so far not been possible to correctly predict needle tissue interactions because of the variability of the soft tissue properties. Interventions with rotating needles are a considerable alternative to provide highly beneficial accuracy in relative studies [41, 42] and we will take this into consideration when studying the next work. In the future, some functions need to be optimized in order to improve the system performance. More phantom and clinical experiments should be done to improve and evaluate the robot system.

Data Availability

All data used to support the findings of this study are available from the corresponding author upon request.

Conflicts of Interest

The authors declare that there are no conflicts of interest regarding the publication of this paper.

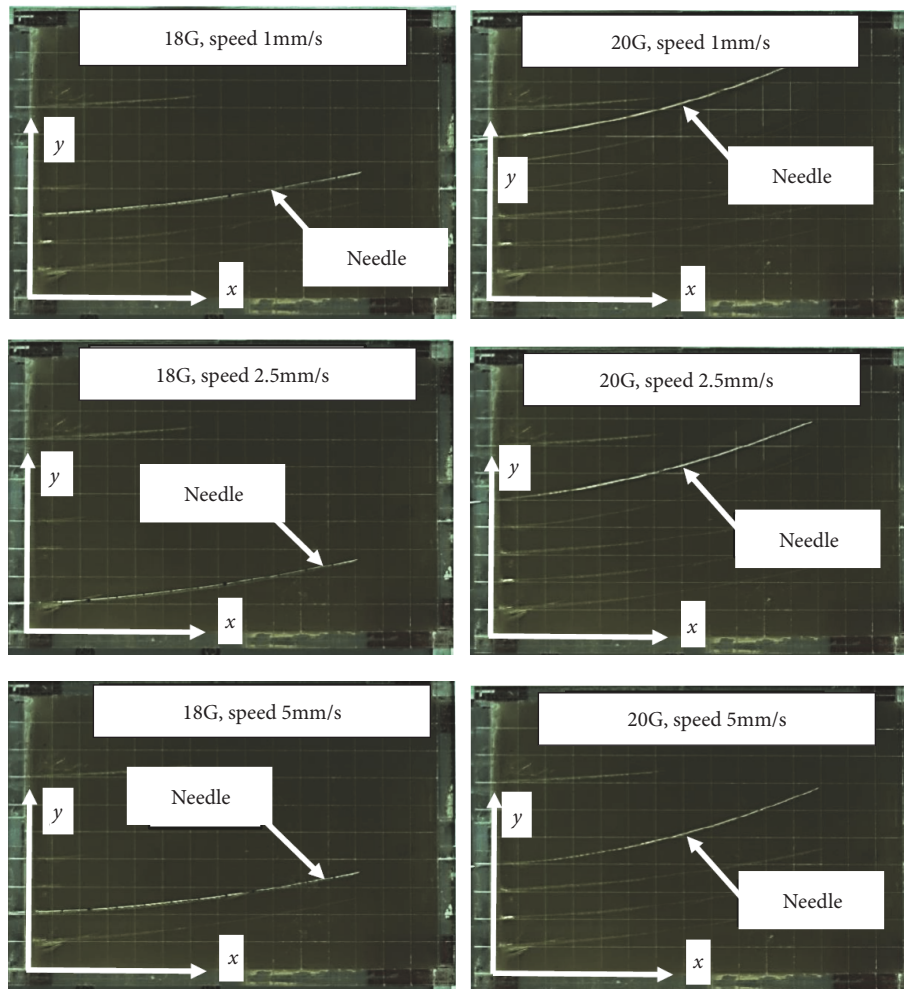


FIGURE 14: The experiment of needle deflection.

Acknowledgments

This research was supported by the National Key R&D Program of China (Grant No. 2017YFB1304302), China Postdoctoral Science Foundation funded project (Grant No. 2018M641216), and National Natural Science Foundation of China (Grant No. 61673064).

References

- [1] B. S. Peters, P. R. Armijo, C. Krause, S. A. Choudhury, and D. Oleynikov, "Review of emerging surgical robotic technology," *Surgical Endoscopy*, vol. 32, no. 4, pp. 1636–1655, 2018.
- [2] L. Yu, X. Chen, and A. Margalit, "Robot-assisted vs freehand pedicle screw fixation in spin surgery – a systematic review and a meta-analysis of comparative study," *International Journal of Medical Robotics and Computer Assisted Surgery*, vol. 14, article 1892, 2018.
- [3] D. P. Losey, C. G. McDonald, E. Battaglia, and M. K. O'Malley, "A review of intent detection, arbitration, and communication aspects of shared control for physical human-robot interaction," *Applied Mechanics Reviews*, vol. 70, 2018.
- [4] M. Hagio, K. Ishizaki, M. Ryu, T. Nomura, N. Takano, and K. Sakurai, "Maxillofacial prosthetic treatment factors affecting oral health-related quality of life after surgery for patients with oral cancer," *Journal of Prosthetic Dentistry*, vol. 119, no. 4, pp. 663–670, 2018.
- [5] H. Boyes, J. Brraclough, and R. Ratansl, "Structured review of the patient-reported outcome instruments used in clinical trials in head and neck surgery," *British Journal of Oral and Maxillofacial Surgery*, vol. 56, pp. 161–167, 2018.
- [6] Y. L. Jiang, N. Meng, J. J. Wang et al., "CT-guided iodine-125 seed permanent implantation for recurrent head and neck cancers," *Radiation Oncology*, vol. 5, article 68, 2010.
- [7] R. Krempien, S. Hassfeld, J. Kozak et al., "Frameless image guidance improves accuracy in three-dimensional interstitial brachytherapy needle placement," *International Journal of Radiation Oncology, Biology, and Physics*, vol. 60, no. 5, pp. 1645–1651, 2004.
- [8] K. T. Kavanagh, "Applications of image-directed robotics in otolaryngologic surgery," *The Laryngoscope*, vol. 104, no. 3, pp. 283–293, 1994.
- [9] T. C. Lueth, A. Hein, J. Albrecht et al., "A surgical robot system for maxillofacial surgery," in *Proceedings of the 24th Annual Conference of the Industrial Electronics Society, IECON '98*, vol. 4, pp. 2470–2475, IEEE, August 1998.
- [10] E. M. Genden, S. Desai, and C.-K. Sung, "Transoral robotic surgery for the management of head and neck cancer: a

- preliminary experience,” *Head and Neck*, vol. 31, no. 3, pp. 283–289, 2009.
- [11] J. C. Selber, “Transoral robotic reconstruction of oropharyngeal defects: a case series,” *Plastic and Reconstructive Surgery*, vol. 126, no. 6, pp. 1978–1987, 2010.
 - [12] T. Theodossy and M. A. Bamber, “Model surgery with a passive robot arm for orthognathic surgery planning,” *Journal of Oral and Maxillofacial Surgery*, vol. 61, no. 11, pp. 1310–1317, 2003.
 - [13] E. A. Z. Omar and M. A. Bamber, “Orthognathic model surgery by using of a passive Robot Arm,” *The Saudi Dental Journal*, vol. 22, no. 2, pp. 47–55, 2010.
 - [14] L. M. Chen, N. Luan, S. L. Zhang et al., “Research on the application of multi DOF robot on orthognathic navigation surgery,” *Mach Electron*, vol. 4, pp. 57–60, 2010.
 - [15] R. Boesecke, J. Brief, J. Raczkowski et al., “Robot assistant for dental implantology,” in *Proceedings of the International Conference on Medical Image Computing and Computer-Assisted Intervention*, pp. 1302–1303, Springer, Berlin, Germany, 2001.
 - [16] X. Sun, F. D. McKenzie, S. Bawab, J. Li, Y. Yoon, and J.-K. Huang, “Automated dental implantation using image-guided robotics: registration results,” *International Journal for Computer Assisted Radiology and Surgery*, vol. 6, no. 5, pp. 627–634, 2011.
 - [17] D. Engel, W. Korb, J. Raczkowski, S. Hassfeld, and H. Woern, “Location decision for a robot milling complex trajectories in craniofacial surgery,” in *Proceedings of the 17th International Congress and Exhibition of Computer Assisted Radiology and Surgery*, 2003.
 - [18] H. Kawana, S. Usuda, K. Yu, T. Nakagawa, and K. Ohnishi, “A remote controlled haptic drilling robot for oral and maxillofacial surgery,” *International Journal of Oral and Maxillofacial Surgery*, vol. 46, article 207, 2017.
 - [19] L. Lin, Y. Shi, A. Tan et al., “Mandibular angle split osteotomy based on a novel augmented reality navigation using specialized robot-assisted arms - A feasibility study,” *Journal of Cranio-Maxillo-Facial Surgery*, vol. 44, no. 2, pp. 215–223, 2016.
 - [20] X. Kong, X. Duan, and Y. Wang, “An integrated system for planning, navigation and robotic assistance for mandible reconstruction surgery,” *Intelligent Service Robotics*, vol. 9, no. 2, pp. 113–121, 2016.
 - [21] N. Nadjmi, “Transoral robotic cleft palate surgery (TORCS),” *The Cleft Palate-Craniofacial Journal*, vol. 44, pp. 114–115, 2015.
 - [22] K. Ohnishi, K. Yu, T. Nakagawa, and H. Kawana, “Automatic stop system for avoiding over cut in implant surgery using haptic drilling robot,” *Journal of Oral and Maxillofacial Surgery*, vol. 72, article 61, 2014.
 - [23] M. Wierzbicka, A. Bartochowska, V. Strnad et al., “The role of brachytherapy in the treatment of squamous cell carcinoma of the head and neck,” *European Archives of Oto-Rhino-Laryngology*, vol. 273, no. 2, pp. 269–276, 2016.
 - [24] M.-W. Huang, J.-G. Zhang, L. Zheng, S.-M. Liu, and G.-Y. Yu, “Accuracy evaluation of a 3D-printed individual template for needle guidance in head and neck brachytherapy,” *Journal of Radiation Research*, vol. 57, no. 6, pp. 662–667, 2016.
 - [25] T. Popescu, A. C. Kacsó, D. Pisla, and G. Kacsó, “Brachytherapy next generation: Robotic systems,” *Journal of Contemporary Brachytherapy*, vol. 7, no. 6, pp. 510–514, 2015.
 - [26] J. Kettenbach and G. Kronreif, “Robotic systems for percutaneous needle-guided interventions,” *Minimally Invasive Therapy & Allied Technologies*, vol. 24, no. 1, pp. 45–53, 2015.
 - [27] R. Seifabadi, F. Aalamifar, I. Iordachita, and G. Fichtinger, “Toward teleoperated needle steering under continuous MRI guidance for prostate percutaneous interventions,” *The International Journal of Medical Robotics and Computer Assisted Surgery*, vol. 12, no. 3, pp. 355–369, 2016.
 - [28] K. Cleary, S. Lim, C. Jun et al., “Robotically assisted long bone biopsy under MRI imaging: workflow and preclinical study,” *Academic Radiology*, vol. 25, no. 1, pp. 74–81, 2018.
 - [29] Z. Du, W. Wang, Z. Yan, W. Dong, and W. Wang, “Variable admittance control based on fuzzy reinforcement learning for minimally invasive surgery manipulator,” *Sensors*, vol. 17, pp. 844–859, 2017.
 - [30] F. Oscari, R. Oboe, O. A. D. Albasini, S. Masiero, and G. Rosati, “Design and construction of a bilateral haptic system for the remote assessment of the stiffness and range of motion of the hand,” *Sensors*, vol. 16, article 1633, 2016.
 - [31] S. Zhang, S. Guo, B. Gao, H. Hirata, and H. Ishihara, “Design of a novel telerehabilitation system with a force-sensing mechanism,” *Sensors*, vol. 15, no. 5, pp. 11511–11527, 2015.
 - [32] M. Bowthorpe, M. Tavakoli, H. Becher, and R. Howe, “Smith predictor-based robot control for ultrasound-guided teleoperated beating-heart surgery,” *IEEE Journal of Biomedical and Health Informatics*, vol. 18, no. 1, pp. 157–166, 2014.
 - [33] J. Dong, L. Zhang, L. Yu et al., “Puncture locating for laparoscopic robot in minimally invasive surgery,” in *Proceedings of the International Symposium on Intelligent Information Technology Application*, pp. 658–662, December 2008.
 - [34] J. Gonzalez-Martinez, S. Vadera, J. Mullin et al., “Robot-assisted stereotactic laser ablation in medically intractable epilepsy: operative technique,” *Neurosurgery*, vol. 10, pp. 167–172, 2014.
 - [35] G. Deacon, A. Harwood, J. Holdback et al., “The pathfinder image-guided surgical robot,” *Proceedings of The Institution of Mechanical Engineers Part H*, vol. 224, no. 5, pp. 691–713, 2010.
 - [36] D. Von Langsdorff, P. Paquis, and D. Fontaine, “In vivo measurement of the frame-based application accuracy of the Neuromate neurosurgical robot,” *Journal of Neurosurgery*, vol. 122, no. 1, pp. 191–194, 2015.
 - [37] J. Kettenbach, L. Kara, G. Toporek, M. Fuerst, and G. Kronreif, “A robotic needle-positioning and guidance system for CT-guided puncture: ex vivo results,” *Minimally Invasive Therapy and Allied Technologies*, vol. 23, no. 5, pp. 271–278, 2014.
 - [38] Q. Duan, Z. Du, H. Yu, Y. Wang, and W. Dong, “Error analysis and experimental study of a Bi-planar parallel mechanism in a pedicle screw robot system,” *Sensors*, vol. 16, pp. 2022–2036, 2016.
 - [39] G. Li, H. Su, W. Shang et al., “A fully actuated robotic assistant for MRI guided prostate biopsy and brachytherapy,” *Proceeding of SPIE-the International Society*, vol. 8671, no. 3, article 867117, 2013.
 - [40] G. Wan, Z. Wei, L. Gardi, D. B. Downey, and A. Fenster, “Brachytherapy needle deflection evaluation and correction,” *Medical Physics*, vol. 32, no. 4, pp. 902–909, 2005.
 - [41] B. L. Davies, S. J. Harris, and E. Dibble, “Brachytherapy - an example of a urological minimally invasive robotic procedure,” *The International Journal of Medical Robotics and Computer Assisted Surgery*, vol. 1, pp. 88–96, 2004.
 - [42] M. A. Meltsner, N. J. Ferrier, and B. R. Thomadsen, “Observations on rotating needle insertions using a brachytherapy robot,” *Physics in Medicine and Biology*, vol. 52, no. 19, pp. 6027–6037, 2007.

